Detection, quantification, and isomer differentiation of per- and polyfluoroalkyl substances (PFAS) using MALDI-TOF with trapped ion mobility

Aidan J. Reynolds[1], Abby M. Smith[1], Tian (Autumn) Qiu[1,2,*]

[1]Department of Chemistry, [2]MSU Center for PFAS Research, Michigan State University, East Lansing, MI 48824, USA

*Corresponding author: Tian (Autumn) Qiu, qiutian8@msu.edu.

Abstract

Per- and polyfluoroalkyl substances (PFAS) are a class of organic compounds that have attracted global attention for their persistence in the environment, exposure to biological organisms, and their adverse health effects. There is an urgent need to develop analytical methodologies for characterization of PFAS in various sample matrices. Matrix-assisted laser desorption/ionization mass spectrometry (MALDI-MS) represents a chromatography-free MS method that performs laser-based ionization and *in situ* analysis on samples. In the present study, we present PFAS analysis by MALDI-time-of-flight MS with trapped ion mobility (TIMS), which provides an additional dimension of gas phase separation based on the size-to-charge ratios. MALDI matrix composition and key instrument parameters were optimized to produce different ranges of calibration curves. Parts per billion range of calibration curves were achieved for a list of legacy and alternative perfluorosulfonic acids (PFSAs) and perfluorocarboxylic acids (PFCAs), while ion mobility spectrum filtering enabled parts per trillion (ppt) range of calibration curves for PFSAs. We also successfully demonstrated the separation of three perfluorooctanesulfonic acid (PFOS) structural isomers in the gas phase using TIMS. Our results demonstrated the new development of utilizing MALDI-TOF-MS coupled with TIMS for fast, quantitative, and sensitive analysis of PFAS, paving ways to future high-throughput and *in situ* analysis of PFAS such as MS imaging applications.

Running title: PFAS analysis with MALDI-TIMS-TOF MS.

Address reprint requests to:

Tian (Autumn) Qiu
Department of Chemistry
578 S Shaw Ln, Room 240
East Lansing, MI 48824
Office: 517-353-1122
Email: qiutian8@msu.edu

1. Introduction

Per- and polyfluoroalkyl substances (PFAS) are a class of persistent environmental contaminants that have been in use since the mid-20th century.[1,2] Due to their high stability and amphiphilic properties, PFAS have been used in various industrial processes and consumer products such as non-stick cookware, firefighting foams, and household cleaning products.[3] Over the past several decades, per- and polyfluorinated compounds have evolved and diversified, resulting in thousands of different chemical structures and functional differences.[4] PFAS have shown resistance to biological and chemical degradation due to their physicochemical properties[5], which has led to accumulation of these compounds in the environment. Their persistence and accumulation in the environment often result in biomagnification within the food chain as you ascend trophic levels.[6-10] Research has shown that PFAS cause adverse health effects such as fertility issues, thyroid disease, and endocrine function.[1,11] There is a significant concern regarding the fate of PFAS in the environment and the long-term adverse effects of PFAS exposure in humans and other organisms, calling for an urgent need for the development of analytical methodologies for characterizing PFAS in a wide variety of samples.

Many analytical advancements have been made to address the challenge of PFAS analysis.[12,13] One particularly important tool is mass spectrometry (MS). Current efforts in MS-based PFAS analysis focus on utilizing liquid or gas chromatography (LC/GC)-MS for qualitative and quantitative characterization of PFAS in complex matrices.[14] While chromatography-coupled MS methodologies enable sensitive detection and comprehensive structural elucidation, they usually require extensive sample preparation, cost longer time in analysis, and may be prone to contaminations during sample processing.[15] Furthermore, LC/GC-MS analysis requires the samples to be homogenized and causes the loss of spatial information. Matrix-assisted laser desorption/ionization (MALDI) is a laser-based "soft ionization" technique for chromatography-free, in situ MS analysis. Coupled with a time-of-flight (TOF) mass analyzer, MALDI-TOF-MS has been widely used for high-throughput and imaging MS applications[16-18]. Some studies have reported the application of MALDI-MS to profile the spatial distribution of PFAS in zebrafish and mouse tissues,[19-22] and detect PFAS in environmental water samples[23], showcasing MALDI-MS as a promising tool for fast, in situ PFAS analysis.

The structural diversity of PFAS and other xenobiotics, together with the complexity of biological and environmental matrices where PFAS are present, calls for the capability to identify PFAS signals from biological molecules and backgrounds. Chromatography, high-resolution and tandem MS, and Kendrick Mass Defect (KMD) analysis are among tools that are widely used.[14,24] In recent years, ion mobility spectrometry (IMS) has shown unique strength in the analysis of halogenated xenobiotics, including PFAS, due to its capability in separating ions by size, shape and charge state in the gas phase.[25-27] By coupling drift-time ion mobility spectrometry (DTIMS) to LC-MS, Foster, et al. demonstrated a unique trendline of collision cross section vs. *m/z* for halogenated xenobiotics compared to biological molecules, facilitating the identification of xenobiotics in a complex sample matrix.[28] Furthermore, DTIMS is capable of differentiating PFAS isobars and isomers.[15] Trapped ion mobility spectrometry (TIMS) is one of the most recent iterations of IMS and facilitates ion separation by using a carrier gas to pass ions through a mobility separation region against an opposing electric field gradient. Ions are eluted after

45 achieving separation by decreasing the opposing electric field; by tuning the ramping time, TIMS
46 can achieve resolution of ~300.[29] Recently, the development of instrumentation has enabled a
47 MALDI-TIMS-TOF configuration,[30] providing opportunities for utilizing the power of IMS with
48 MALDI-MS for PFAS analysis.
49
50 Herein, we establish a MALDI-TIMS-TOF method for quantitative analysis of several legacy and
51 alternative PFAS molecules. Matrix screening and optimization was performed for negative
52 ionization mode analysis for selected legacy and alternative perfluorocarboxylic acids (PFCAs)
53 and perfluorosulfonic acids (PFSAs), which demonstrated that 1,5-diaminonaphthalene was best
54 suited for PFAS analysis. Several key instrument parameters were tuned and optimized to
55 maximize detection and sensitivity of PFAS analysis by MALDI-TIMS-TOF with detection and
56 quantitation for PFCAs and PFSAs at ppb and ppt concentrations, respectively. Mobility filtering
57 by TIMS improved S/N by reducing background signal in select PFSAs examined at ppt
58 concentrations. Furthermore, we've firstly reported differentiation of PFAS structural isomers
59 using TIMS. Our results demonstrated the new development of utilizing MALDI-TOF-MS coupled
60 with TIMS for fast, quantitative, and sensitive analysis of PFAS, paving ways to future high-
61 throughput and *in situ* analysis of PFAS such as MS imaging applications.
62
63 **2. Materials and Methods**
64
65 *2.1 Materials*
66 Perfluorohexanoic acid (PFHxA, >98%), perfluorodecanoic Acid (PFDA, 98%), perfluoro-3,7-
67 dimethyloctanoic acid (PF-3,7-DMOA, 95%), perfluorobutanesulfonic acid (PFBS, 97%), and
68 ammonium 2,3,3,3-tetrafluoro-2-(heptafluoropropoxy)propanoate (GenX, 95%), 2',5'-
69 dihydroxyacetophenone (2',5'-DHAP, 97%), 2',6'-dihydroxyacetophenone (2',6'-DHAP, 99%), 9-
70 aminoacridine (9-AA, >99.5%), norharmane (NRM, 98%) were purchased from Sigma-Aldrich
71 Chemical (St. Louis, MO, USA). Sodium perfluoro-3-methylheptanesulfonate
72 (Na3PMHpS, >98%), sodium perfluoro-6-methylheptanesulfonate (Na6PMHpS, >98%), and
73 potassium 9-chlorohexadecafluoro-3-oxanonane-1-sulfonate (F53B (Major), >98%) were
74 purchased from Wellington Laboratories (Guelph, Ontario, Canada). Perfluorooctanoic acid
75 (PFOA, 96%), 1',8'-Bis(dimethylamino)napthalene (DMAN), 1',5'-diaminonaphthalene
76 (DAN, >98%), LC-MS grade acetonitrile, LC-MS grade water, and LC-MS grade methanol were
77 purchased from Fisher Scientific (Pittsburgh, PA, USA). Perfluorohexanesulfonic acid
78 (PFHxS, >95%), and perfluorooctanesulfonic acid (PFOS, >97%) were purchased from Synquest
79 Labs (Alachua, FL, USA).
80
81 *2.2 Sample Preparation*
82 Chemical matrices were prepared to 1mL total volumes, and each matrix was vortexed prior to
83 aliquoting. Matrices were dissolved as follows: DAN at 10 mg/mL in 7:3 acetonitrile:water, 9-AA
84 at 10 mg/mL in 9:1 methanol:water, 2',5'-DHAP at 15 mg/mL in 8:2 acetonitrile:water, 2',6'-DHAP
85 at 10 mg/mL in 1:1 acetonitrile:water, DMAN at 10 mg/mL in 100% acetonitrile and NRM at 10
86 mg/mL in 7:3 methanol:water. All solvents are LC-MS grade. For each PFAS, two stock
87 concentrations were prepared: 1 µg/mL (ppm) and 1 ng/mL (ppb). All PFAS excluding F53B
88 (major) were prepared by dissolution in water to yield a 1mg/mL solution. Immediately after, a

89   1000-fold dilution was performed by transferring 10 μL of the 1mg/mL solution and diluting to 10

90   mL total volume in water to yield a 1 µg/mL (ppm) solution. From this 1 µg/mL solution, another

91   1000-fold serial dilution was performed, again by transferring 10 μL from the 1 µg/mL solution and

92   diluting to a final volume of 10 mL, yielding a 1 ng/mL (ppb) solution. A 1.2 mL methanol ampule

93   containing 50 µg/mL of F53B (major) was diluted 5-fold using water to a final volume of 6 mL to

94   yield a 10 µg/mL concentration. From this solution, a 10-fold dilution using water was performed

95   to produce a 1 µg/mL (ppm) solution. From this solution, a 1000-fold dilution using water was

96   performed by transferring 10 μL from the 1 µg/mL solution and diluting to a final volume of 10 mL.

97   All stock solutions were prepared in water and stored in polypropylene conical tubes. Standards

98   were made immediately before each experiment and vortexed prior to aliquoting. Sub-ppm

99   standards of 750, 500 and 250 ppb were prepared by serial dilution from a 1-ppm stock solution.

100   A 100-ppb standard was prepared by parallel dilution from the 1-ppm stock, and the 50-ppb and

101   10-ppb standards were prepared by serial dilution from the 100-ppb standard. Sub-ppb standards

102   were prepared by serial dilution only from a 1-ppb sub-stock solution. Standards were diluted

103   using a 1:1 methanol:water solution. Organic solvent was added to diluent to increase the rate of

104   spot-drying and improve matrix crystal homogeneity on target plate.

105

106   *2.3 MALDI-TIMS-TOF Analysis*

107   MALDI parameters in TIMS-mode were optimized to maximize PFAS signal intensity from 150

108   *m/z* to 700 *m/z*. Laser parameters used in data collection include: M5 defocused MS dried droplet

109   laser focusing, a laser frequency of 10,000Hz, and 25 laser shots per burst. Ion optics parameters

110   were also tuned, including a collision cell energy of 10.0 eV, a collision RF of 750.0 Vpp, an ion

111   transfer time of 50.0 µs, a pre pulse storage time of 5 µs, a TIMS funnel 1 RF of 300.0 Vpp, a

112   TIMS funnel 2 RF of 200.0 Vpp, a Multipole RF of 200.0 Vpp, a Deflection 1 Delta of -70.0V, a

113   Δt4 (Accumulation Trap -> Funnel 1 In) of -25.0 V, a Δt6 (Ramp Start -> Accumulation Exit) of -

114   25.0 V, and a collision cell in voltage of -140.0 V.

115

116   For MALDI-TIMS-TOF analysis, spotting technique was used. All spotting was performed by

117   transferring 0.5 µL of analyte onto a ground steel Bruker MTP target plate, followed by overlaying

118   a drop of 0.5 µL matrix solution onto the analyte drop. Samples were allowed to dry at ambient

119   temperature, and the formation of crystals was observed under a Zeiss Stemi 305

120   stereomicroscope. For matrix screening, spots were prepared in technical replicates of n=3 and

121   randomly sampled 20 times at different locations on the spot for a total of 500 shots. Isomer

122   differentiation spots were randomly sampled 8 times for a total of 200 shots. Sub-ppm and sub-

123   ppb standards were spotted in technical replicates of n=5 and randomly sampled 20 times for a

124   total of 500 shots at laser intensities of 20% and 50%, respectively. The spots were analyzed in

125   negative-ion mode from 150 *m/z* to 1100 *m/z.*

126

127   *2.4 Data Analysis*

128   Mass spectra were analyzed using Bruker Compass DataAnalysis Version 6.1 and processed

129   using Microsoft Excel 2019. Spectrum Data was copied from DataAnalysis and pasted into a

130   Microsoft Excel template. Data in Microsoft Excel was filtered to identify *m/z* that belonged to

131   PFAS. **Figure 1** and **Table 1** contains data analysis from unnormalized, raw peak intensity in the

132   mass spectra. In **Figure 1**, for easier visualization, logarithmic transformation was performed due

133 to there being several orders of magnitude differences in analyte raw intensities across matrices.
134 S/N ratio was calculated based on raw spectra. The average and standard deviation of the
135 baseline intensities adjacent to analyte peaks were determined by sampling 10 background
136 intensities within the range ±3 x (the width at the analyte's peak base). Signal-to-noise ratio (S/N)
137 of the analyte peak was established by subtracting the mean baseline intensity surrounding
138 analyte peaks from the observed analyte intensity and dividing by the standard deviation of the
139 baseline signal. Standard deviation of S/N ratios for technical replicates were calculated using the
140 STDEV.S function in Excel.
141
142 For **Table 1**, we estimated LOD/LOQ values from raw mass spectra (sub-ppm) and mobility-
143 filtered mass spectra (sub-ppb). For sub-ppm range, the raw peak intensities from the mass list
144 of raw mass spectra were used to represent analyte signals. For sub-ppb range, mobility filtering
145 was performed to extract a filtered analyte peak intensity. Extracted ion mobility (EIM) of the
146 analyte was performed from the raw mobility-*m/z* spectrum by filtering the mobilogram at analyte
147 *m/z* ± 10 ppm. The mobility peak (Compounds) corresponding to the analyte was identified by the
148 DataAnalysis and then selected to show the mass spectrum filtered by the range of the Compound
149 peak. The filtered intensity of analyte was used to represent mobility-filtered analyte peak
150 intensity. With the analyte peak intensity, linear regressions were performed on their averages of
151 the technical replicates; standards with average S/N < 10 were not included for linear regression.
152 Estimated LOD and LOQ intensities were established as 3 standard deviations and 10 standard
153 deviations above background noise present in blanks, respectively. Estimated LOD and LOQ
154 concentrations were calculated by dividing the LOD and LOQ intensities to slopes of the best fit
155 lines produced from analyte peak intensities. Slopes produced by intensities from multi-day
156 calibration curve trials, LOQ, LOD and S/N ratios were averaged with variation described as
157 relative standard deviation percentage (RSD%).
158
159 We then performed total ion current (TIC) normalization to help reduce variations across
160 replicates and build calibration curves using the standards with average S/N > 10 that were
161 identified from raw spectra. TIC was calculated by summing all intensities in the mass list found
162 by DataAnalysis in each raw mass spectrum. TIC normalization was performed by dividing analyte
163 peak raw intensity (sub-ppm, **Figure 2**) or mobility-filtered analyte peak intensity (sub-ppb, **Figure
164 3**) by the TIC. TIC normalized analyte signals were averaged across technical replicates using
165 the AVERAGE function, and standard deviation of the replicate sample sets were calculated using
166 the STDEV.S function. Relative standard deviation percentage (RSD%) was calculated by
167 dividing the standard deviation of replicates by the mean and converted to a percentage value.
168
169 ## 3. Results and Discussion
170
171 **Matrix screening showed DAN as a suitable matrix for all selected PFAS.** Matrix selection is
172 essential for efficient energy transfer from laser to analyte and should be capable of ionizing
173 analytes by protonation or deprotonation.[31] Several commonly used matrices (DMAN, 2,6-DHAP,
174 DAN, 2,5-DHAP, 9-AA, NRM) for negative ion mode analysis were chosen for the detection of
175 PFCAs and PFSAs. Preliminary investigation into these matrices revealed that DMAN and 2,6-
176 DHAP had poor vacuum stability and were prone to sublimation, rendering them unusable in this

177   study. Four PFAS were chosen as representatives for both PFCA and PFSA families: GenX,
178   PFDA, PFBS and PFOS. As shown in **Figure 1A**, DAN was the only matrix to produce signals
179   that could be attributed to all four PFAS and produced the highest intensities and S/N ratios across
180   all PFAS screened. When comparing spectra of each PFAS across matrices, PFCAs showed
181   significant fragmentation when DAN was used as the matrix whereas PFSA showed minimal
182   fragmentation. Similarly reported by Cao et al., PFDA produced signals at *m/z* 468.9696 [M–
183    $CO_2H]^-$ and *m/z* 430.9728 [M–2F–$CO_2H]^-$ in addition to *m/z* 512.9594 [M–H]$^-$ (**Figure S1A**).[22]
184   Notably, the [M–2F–$CO_2H]^-$ peak appeared to be the highest among all PFDA peaks. NRM
185   induced some fragmentation with PFDA, yielding only [M–$CO_2H]^-$ and [M–H]$^-$ signals to be
186   detected (**Figure S1B**). 2,5-DHAP only yielded molecular ion peaks and no fragmentation ions
187   were detected, which may be related to the low intensity of its molecular ion peak (**Figure S1C**),
188   and 9-AA did not produce observable PFDA peaks (**Figure S1D**). Contrary to PFDA, GenX
189   showed no [M–H]$^-$, [M– $CO_2H]^-$, or [M–2F–$CO_2H]^-$ related peaks. Instead, fragmentation
190   occurred at the ether present in the fluorinated chain to produce a signal at *m/z* 184.9837 which
191   corresponds to the formula [$C_3F_7O]^-$ (**Figure S1E**). To further investigate the detection sensitivity
192   of these matrices, concentrations for each PFAS were reduced to 1ppb. Illustrated by **Figure 1B**,
193   PFCAs were not detected across all matrices, however, both PFSAs were still detectable with
194   DAN. Thus, DAN was chosen as the chemical matrix for PFAS analysis for the subsequent
195   experiments.

196

197
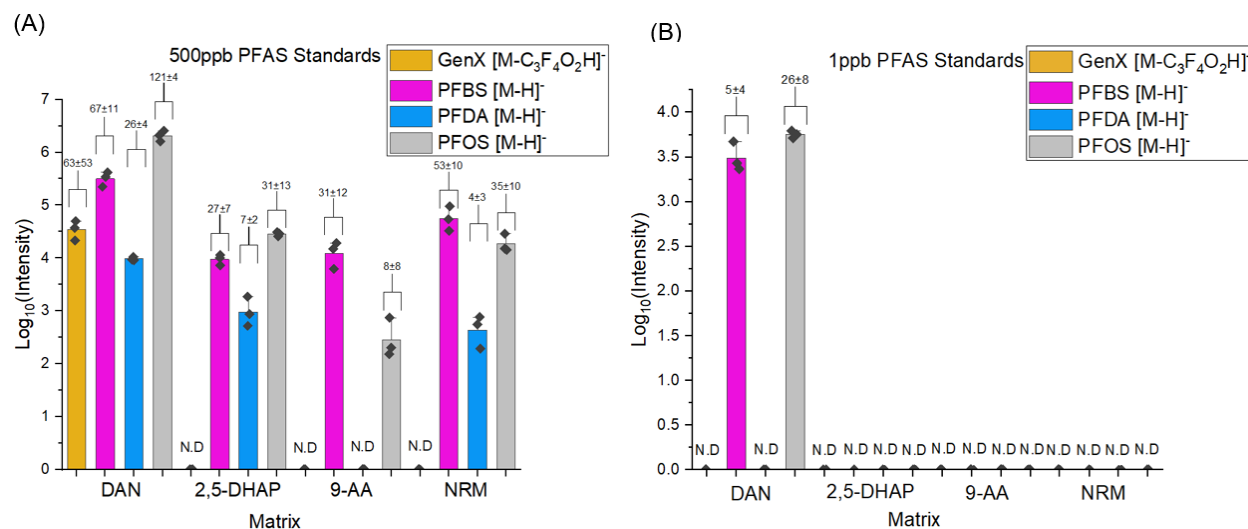
198   **Figure 1**. Matrix screening for (A) 500 ppb and (B) 1 ppb of PFAS solution. Different colored bars
199   represent the average signal intensities of ions from a specific PFAS, and solid diamonds indicate
200   individual replicates (n=3). Error bars represent standard deviation. Numbers above each bar
201   indicate the S/N ratio of the signal of interest from raw spectra (average ± SD). Regions labeled
202   N.D represent nondetectable signals with S/N<3. The Y-axis is plotted in logarithmic scale.

203

204   **Multi-day calibration curves demonstrated PFAS quantification at different ranges.** Matrix
205   optimization data demonstrated parts per billion detection and quantification for select PFCA and
206   PFSA. To investigate the quantitative capability of MALDI-TIMS-TOF detection, calibration curves
207   of sub-ppm and sub-ppb ranges for PFAS compounds were prepared in technical replicates (n=5),

208 and the calibration curve was freshly made for repeated analysis for at least three times across
209 multiple days. The results were summarized in **Table 1** and illustrated in **Figure 2 and 3**. Of the
210 calibration curves analyzed, one GenX calibration curve was excluded due to erroneous standard
211 preparation, where significantly different peak intensities and linearity were observed. It should
212 be noted that the calibration curves for sub-ppm and sub-ppb are not directly comparable due to
213 the different laser intensities used for different concentration ranges. From **Table 1**, it is clear that
214 the slopes of calibration curves (sensitivity) and LOD/LOQ greatly differ among PFAS types. For
215 sub-ppm range, PFSAs showed better detection with orders of magnitude higher sensitivities and
216 lower LOD/LOQ values compared to PFCAs. We observed that among different chain lengths of
217 legacy PFCA and PFSA series, PFOA and PFOS showed the best detection with highest slope
218 and smallest LOD/LOQ. This may be attributed to the TIMS parameters we optimize that prefer
219 the middle part of the calibration range (150-1100 *m/z*). The reproducibility of sub-ppm and sub-
220 ppb calibration curves with multi-day experiments are evaluated by the slopes and their RSD%
221 values (**Table 1**). Most of the RSD% of slopes determined from multi-day experiments were
222 around 30%, which was expected considering the semi-quantitative nature of MALDI-MS
223 analysis. It should be noted that normalization by TIC did not seem to reduce the RSD% of slope
224 across days (**Table S1**). Reproducibility may be improved by using internal standards and
225 improving the homogeneity of matrix crystals.[32] Spotting method for matrix application may cause
226 heterogenous crystal formation; a spray-coating or sublimation application technique can be used
227 to improve crystal heterogeneity.

229 The individual sub-ppm calibration curves for PFCAs were plotted in **Figure 2A-D**. Across all
230 legacy PFCAs tested (PFHxA, PFOA, and PFDA), $[M–2F–CO_2H]^-$ peaks yielded the highest
231 signal intensity, followed by $[M–CO_2H]^-$ peaks with $[M–H]^-$ peaks producing the least signal
232 intensity (**Figure S1A**). Knowing this, $[M–2F–CO_2H]^-$ signals were used as the signal for
233 quantification in calibration curves with the exception of GenX whose only signal was an ion with
234 the putative fragment $[M-C_3F_4O_2]^-$. Such fragmentation may be attributed to the metastable ions
235 formed from MALDI ionization. As fragmentation results in a series of ions at different *m/z*, it may
236 also contribute to the decreased sensitivity of PFCAs compared to PFSAs, which primarily formed
237 molecular ions. Shown in **Table 1** and **Figure 2E-H**, PFSAs demonstrated greater sensitivity and
238 lower LOD/LOQ compared to PFCAs. All PFSA indicated potential for parts per trillion limits of
239 detection based on LOD/LOQs calculated based on the calibration curves. As observed in GenX
240 where fragmentation occurred at the site of the ether present in the fluorinated chain,
241 fragmentation at this site in F53B (Major) was also observed at *m/z* 350.9446 (**Figure S1F**). In
242 contrast to GenX, this fragment ion was of low intensity, with the dominant ion peak being the $[M–$
243 $H]^-$ signal.

252

253 **Table 1**. Sensitivity, limit of detection/quantification, and S/N ratios from multi-day experiments.

Sub-ppm calibration curves. Values shown as average (RSD%)[#]

		Slope (peak intensity vs. concentration)	Calculated LOD (ppb)[*]	Calculated LOQ (ppb)[*]	Lowest standard with average S/N≥10 (ppb)[**]	S/N of the lowest concentration tested (10 ppb)
PFCA	GenX	31.5 (60.3%)	7 (40.7%)	22 (40.7%)	50	5 (11.8%)
	PFHxA	8.45 (31.3%)	50 (46.2%)	165 (46.2%)	250	3 (27.4%)
	PFOA	103 (29.1%)	3 (29.9%)	8 (29.9%)	50	7 (18.0%)
	PFDA	50.8 (66.4%)	5 (87.3%)	17 (87.3%)	10	10 (49.4%)
PFSA	PFBS	528 (27.7%)	0.96 (106%)	3.22 (106%)	10	13 (26.7%)
	PFHxS	652 (19.1%)	0.19 (22.3%)	0.64 (22.3%)	10	30 (50.8%)
	PFOS	977 (36.2%)	0.08 (30.4%)	0.25 (30.4%)	10	36 (14.5%)
	F53B	750 (49.7%)	0.06 (68.1%)	0.18 (68.1%)	10	28 (49.7%)

Sub-ppb calibration curves. Values shown as average (RSD%)[#]

|		Slope (peak intensity vs. concentration)	Calculated LOD (ppt)[*]	Calculated LOQ (ppt)[*]	Lowest standard with average S/N≥10 (ppt)[**]	S/N of the lowest concentration tested (100 ppt)
PFSA	PFBS	27.2 (38.9%)	34 (101%)	112 (101%)	100	21 (25.1%)
	PFHxS	36.3 (30.6%)	24 (58.4%)	82 (58.4%)	100	20 (25.3%)
	PFOS	97.6 (21.8%)	6 (47.5%)	20 (47.5%)	100	20 (4.91%)
	F53B	30.7 (27.9%)	22 (97.6%)	74 (97.6%)	100	23 (34.4%)

254 [#] Average and RSD calculated from triplicates of calibration curves from multiple days. For sub-ppm range, raw peak
255 intensities of analytes were used. For sub-ppb range, mobility-filtered peak intensities of analytes were used.
256 [*] LOD was calculated using 3*blank SD/slope and LOQ was calculated using 10*blank SD/slope.
257 [**] Lowest calibrant with an average S/N≥10 measured across all multi-day experiments.

258

259
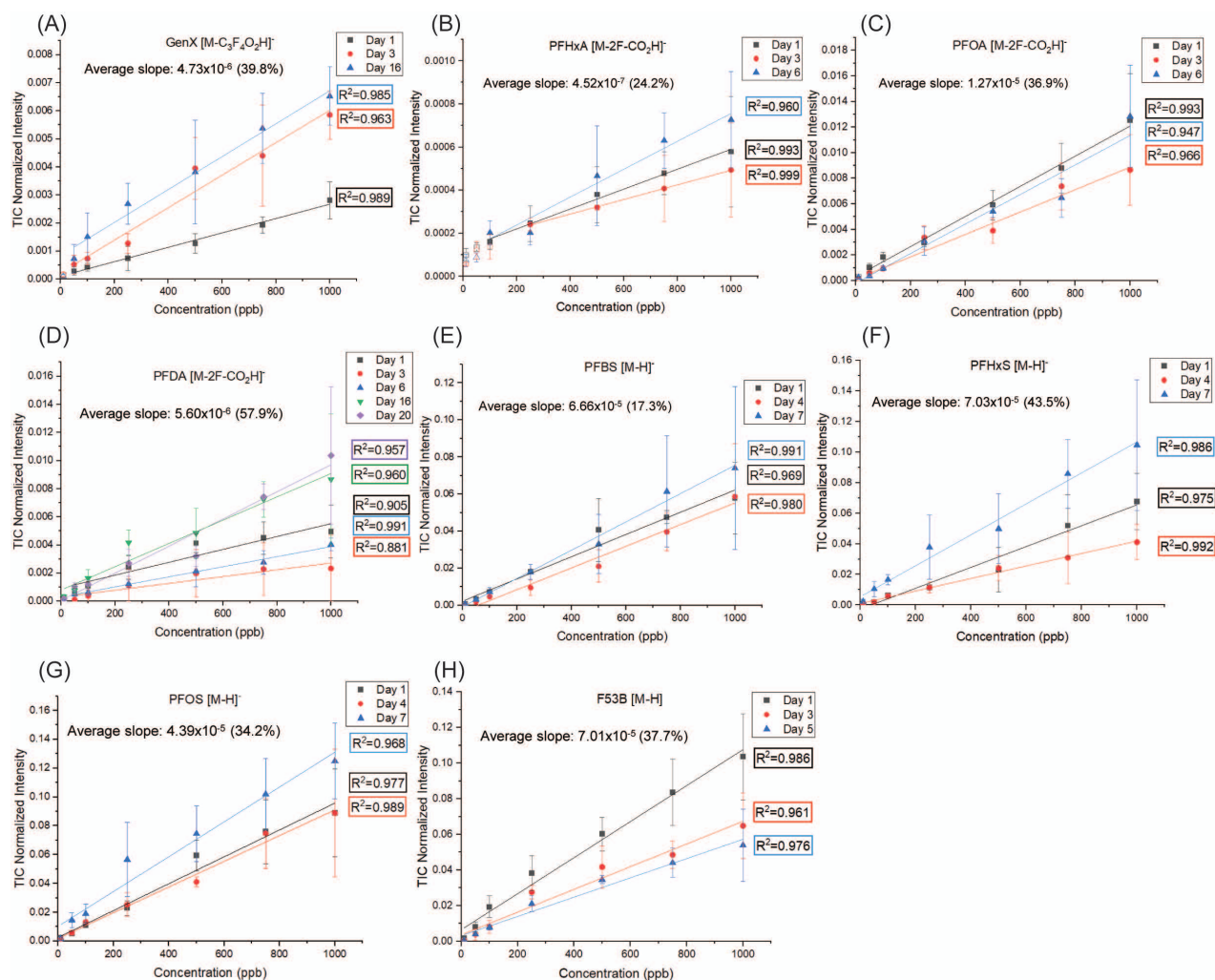
Figure 2. Sub-ppm calibration curves for (A-D) PFCAs and (E-H) PFSAs. Data points represent average normalized intensity from the five replicates in each experiment, and error bar represents standard deviation. Solid shapes indicate data points with average S/N of raw spectra over 10 and used for linear regression of calibration curves. Hollow shapes represent detectable data points with S/N less than 10 and not included for linear regression. Averages and RSD% for multi-day TIC normalized slopes are presented below each calibration curve.

Ion mobility spectrum filtering enabled quantification at sub-ppb (ppt) range. Based on the S/N and calculated LOD/LOQ of PFSA calibrants, we further explore the detection of PFSAs in the parts per trillion (ppt) range. To improve the lower limits of detection and quantitation, laser intensity was increased from 20% to 50%, and mobility filtering was performed to reduce background signal in the mass spectra. Perfluorinated molecules were reported to separate in the CCS-*m/z* 2D space due to the high mass of fluorine atoms, and our TIMS-MS spectra matched the trends reported in DTIMS (**Figure S2**).[28] Results showed that filtering the mass spectrum by the mobility range of analytes of interest successfully decreased the backgrounds and increased detection sensitivity (**Figure 3A, Figure S3**). Notably, upon mobility filtering of blanks (**Figure S3**), it was found that PFAS-associated signal intensities were still present, indicating that TIMS

279 can be used to identify cross-contamination that would otherwise be indistinguishable from non-
280 mobility filtered intensities. With that, we performed mobility filtering for all sub-ppb mass spectra
281 of PFSA to build calibration curves from the multi-day experiments. Shown in **Figure 3B-E** and
282 **Table 1**, calibration curves were built in the ppt range, with limits of detection at low parts per
283 trillion levels. We noticed that the slopes were comparable for PFOS and F53B (Major) at sub-
284 ppm concentrations, but at sub-ppb concentrations F53B (Major) yielded relatively lower slopes
285 compared to PFOS. It is suspected that as laser intensity increased from 20% to 50%,
286 fragmentation at the ether present in the fluorinated chain of F53B (Major) increased, thereby
287 decreasing the intensity and subsequently, the sensitivity of the $[M-H]^-$ base peak.
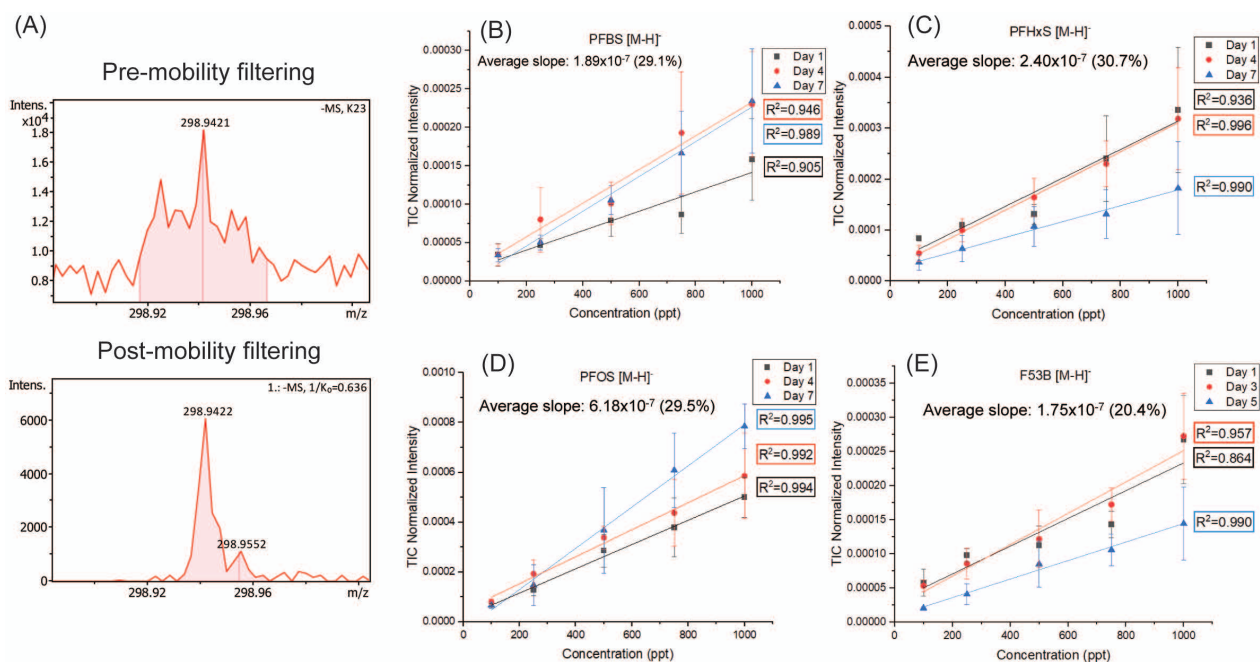
Figure 3. Sub-ppb calibration curves for PFSAs. (A) An example of comparison between pre- and post-mobility filtering for PFBS $[M-H]^-$ ion. (B-E) Calibration curves for PFBS, PFHxS, PFOS and F53B. Data points represent average normalized intensity from the five replicates in each experiment, and error bar represents standard deviation. Solid shapes indicate data points with average S/N of raw spectra over 10 and used for linear regression of calibration curves. Hollow shapes represent data points with S/N less than 10 and not included for linear regression. Averages and RSD% for multi-day TIC normalized slopes are presented below each calibration curve.

Ion mobility and fragmentation patterns allowed differentiation of PFAS structural isomers.
301 It was demonstrated by Spraggins et al. that TIMS could differentiate isobaric lipid species.[30]
302 Isomer differentiation by TIMS was evaluated using three PFSA isomers and two PFCA isomers:
303 PFOS, sodium perfluoro-3-methylheptanesulfonate (Na3PMHpS) and sodium perfluoro-6-
304 methylheptanesulfonate (Na6PMHpS), PFDA and perfluoro-3,7-dimethyloctanoic acid (PF-3,7-
305 DMOA). Improved isomer separation was achieved by reducing the mobility window to 0.65-0.90

306   and increasing ramp time to allow greater separation by TIMS. It should be noted that reducing
307   the mobility window compromised mobility calibration as the detection window no longer contains
308   enough calibrants in the Agilent Tune Mix. As shown in **Figure 4A**, PFOS isomer differentiation
309   was sufficiently achieved using 300ms ramp time and further improved when increased to 800ms.
310   Upon increasing ramp time, it was discovered that the non-analytical standard linear PFOS
311   compound contained isomeric impurities (**Figure 4A**, red trace at the bottom mobilogram). These
312   impurities can affect the quality of analytical testing with MS and affect downstream toxicological
313   assays. Therefore, these factors should be taken into consideration when procuring perfluorinated
314   compounds for research purposes. PFOS isomers were measured at each ramp time individually
315   to confirm peak identity in the mixture. As expected, Na3PMHpS had the smallest measured ion
316   mobility given it was the least bulky ion, followed by Na6PMHpS and lastly, PFOS. Two-peak
317   resolution (R_{pp}) was calculated to measure the degree of separation between Na3PMHpS and
318   Na6PMHpS, as well as Na6PMHpS and PFOS. Maximum R_{pp} for Na3PMHpS/Na6PMHpS and
319   Na6PMHpS/PFOS was achieved using an 800ms ramp time and was calculated to be 0.907 and
320   0.787, respectively. Isomer differentiation was achieved from a 1-ppm mixture of all PFOS at
321   equal concentrations of 333-ppb for each isomer. At low concentrations, isomer differentiation
322   became significantly more challenging due to sensitivity issues.
323
324   Isomer differentiation with TIMS was also explored to differentiate PFDA and PF-3,7-DMOA, a
325   branched isomer of linear PFDA. Different from PFSA like PFOS, PFCAs have thus far
326   demonstrated significant fragmentation when ionized with DAN, which allowed for multiple ion
327   peaks to be utilized for differentiation by mobility filtering. Illustrated by **Figure 4B**, PFDA and PF-
328   3,7-DMOA yielded significantly different fragmentation patterns which prevented direct
329   comparison of ion mobilities due to differences in signal intensity. Contrary to all linear legacy
330   PFCA examined thus far, PF-3,7-DMOA's dominant ion signal appeared to be $[M-CO_2H]^-$ rather
331   than $[M-2F-CO_2H]^-$. Due to the significant difference in ion fragment formation, EIM filtering was
332   not applicable, however, utilizing these "diagnostic fragment" intensities can allow for identification
333   of isomers based on a ratio of intensities,[33] which will be explored in future investigations.
334
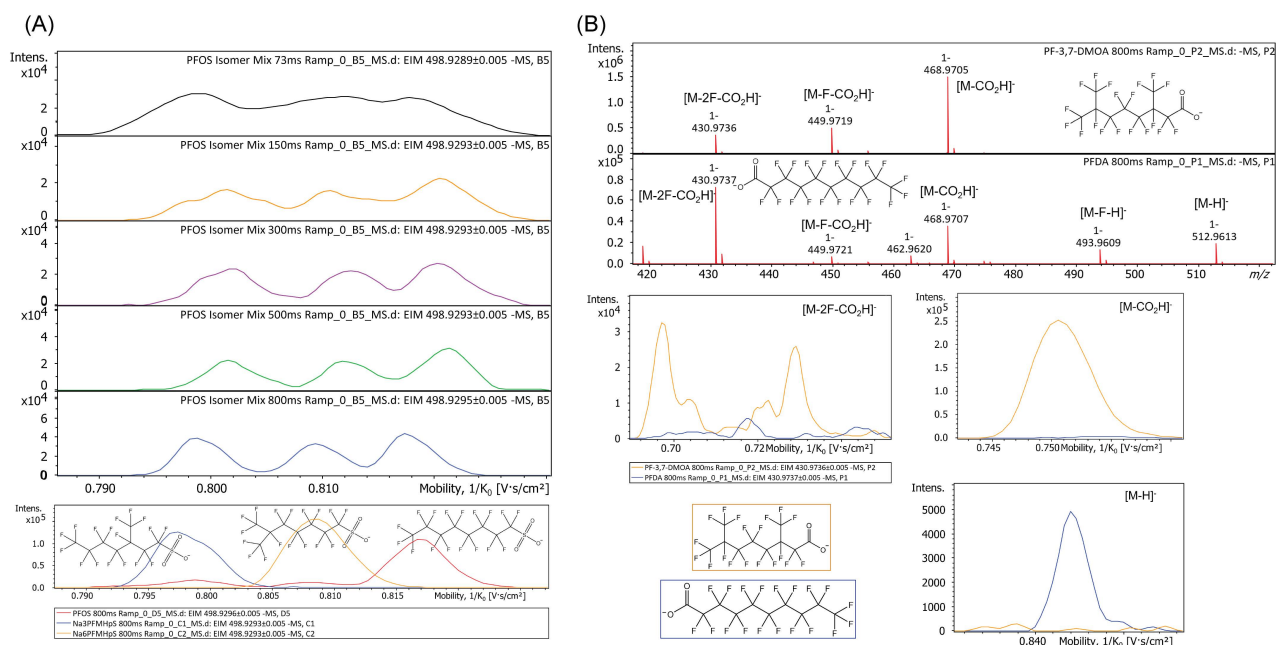
Figure 4. Isomer differentiation with TIMS for (A) PFOS and (B) PFDA isomers. Structures of different isomers are shown. (A) The top five show mobilograms with increasing ramp time from 73 to 800 ms for the separation of three PFOS structural isomers. Bottom panel shows the mobilogram of three individual PFOS isomer standards at 800-ms ramp time, marked with different colors and corresponding structures. (B) The top two mass spectra show different fragmentation patterns of two PFDA structural isomers. The extracted mobilograms of selected fragments and molecular ions are individually shown with colors marking different isomers.

4. Conclusions

We developed a MALDI-TIMS-TOF MS method for the analysis of a list of PFAS that allowed for parts per billion and parts per trillion detection and quantification of select PFCAs and PFSAs, respectively. The timsTOF fleX instrument was optimized for analysis of PFAS in relevant *m/z* and mobility ranges. Matrix screening at negative mode indicated DAN (1',5'-diaminonaphthalene) to be the optimal matrix suitable for all PFSAs and PFCAs tested in this study, although other options may achieve less fragmentations of PFCAs. We generated multi-day calibration curves; without the usage of internal standards, we achieved good linearity in the concentration range we tested and showed reproducibility that reflects the semi-quantitative nature of MALDI-MS analysis. By filtering the mass spectra with the mobilities of specific PFAS analytes, we were able to decrease background and increase the sensitivity of detection. Finally, we achieved differentiation of structural PFOS isomers using TIMS and also showed different fragmentation patterns of PFDA isomers, which may be used as diagnostic patterns for isomer differentiation. Our results showed the potential of MALDI-TIMS-TOF MS analysis as a promising method for in situ, high-throughput analysis of PFAS with low detection limit and capability of isomer differentiation.

6. Citations

1. Fenton, S. E.; Ducatman, A.; Boobis, A.; DeWitt, J. C.; Lau, C.; Ng, C.; Smith, J. S.; Roberts, S. M. Per- and Polyfluoroalkyl Substance Toxicity and Human Health Review: Current State of Knowledge and Strategies for Informing Future Research. *Environ Toxicol Chem* **2021**, *40* (3), 606–630. https://doi.org/10.1002/etc.4890.

2. Kurwadkar, S.; Dane, J.; Kanel, S. R.; Nadagouda, M. N.; Cawdrey, R. W.; Ambade, B.; Struckhoff, G. C.; Wilkin, R. Per- and Polyfluoroalkyl Substances in Water and Wastewater: A Critical Review of Their Global Occurrence and Distribution. *Science of The Total Environment* **2022**, *809*, 151003. https://doi.org/10.1016/j.scitotenv.2021.151003.

3. Teymourian, T.; Teymoorian, T.; Kowsari, E.; Ramakrishna, S. A Review of Emerging PFAS Contaminants: Sources, Fate, Health Risks, and a Comprehensive Assortment of Recent Sorbents for PFAS Treatment by Evaluating Their Mechanism. *Res Chem Intermed* **2021**, *47* (12), 4879–4914. https://doi.org/10.1007/s11164-021-04603-7.

4. Kwiatkowski, C. F.; Andrews, D. Q.; Birnbaum, L. S.; Bruton, T. A.; DeWitt, J. C.; Knappe, D. R. U.; Maffini, M. V.; Miller, M. F.; Pelch, K. E.; Reade, A.; Soehl, A.; Trier, X.; Venier, M.; Wagner, C. C.; Wang, Z.; Blum, A. Scientific Basis for Managing PFAS as a Chemical Class. *Environ. Sci. Technol. Lett.* **2020**, *7* (8), 532–543. https://doi.org/10.1021/acs.estlett.0c00255.

5. Cousins, I. T.; DeWitt, J. C.; Glüge, J.; Goldenman, G.; Herzke, D.; Lohmann, R.; Ng, C. A.; Scheringer, M.; Wang, Z. The High Persistence of PFAS Is Sufficient for Their Management as a Chemical Class. *Environ. Sci.: Processes Impacts* **2020**, *22* (12), 2307–2312. https://doi.org/10.1039/D0EM00355G.

6. Dickman, R. A.; Aga, D. S. A Review of Recent Studies on Toxicity, Sequestration, and Degradation of per- and Polyfluoroalkyl Substances (PFAS). *Journal of Hazardous Materials* **2022**, *436*, 129120. https://doi.org/10.1016/j.jhazmat.2022.129120.

7. Zhang, Z.; Sarkar, D.; Biswas, J. K.; Datta, R. Biodegradation of Per- and Polyfluoroalkyl Substances (PFAS): A Review. *Bioresource Technology* **2022**, *344*, 126223. https://doi.org/10.1016/j.biortech.2021.126223.

8. Lesmeister, L.; Lange, F. T.; Breuer, J.; Biegel-Engler, A.; Giese, E.; Scheurer, M. Extending the Knowledge about PFAS Bioaccumulation Factors for Agricultural Plants – A Review. *Science of The Total Environment* **2021**, *766*, 142640. https://doi.org/10.1016/j.scitotenv.2020.142640.

9. Burkhard, L. P. Evaluation of Published Bioconcentration Factor (BCF) and Bioaccumulation Factor (BAF) Data for Per- and Polyfluoroalkyl Substances Across Aquatic Species. *Environ Toxicol Chem* **2021**, *40* (6), 1530–1543. https://doi.org/10.1002/etc.5010.

10. Death, C.; Bell, C.; Champness, D.; Milne, C.; Reichman, S.; Hagen, T. Per- and Polyfluoroalkyl Substances (PFAS) in Livestock and Game Species: A Review. *Science of The Total Environment* **2021**, *774*, 144795. https://doi.org/10.1016/j.scitotenv.2020.144795.

411

412 11. Flynn, R. W.; Chislock, M. F.; Gannon, M. E.; Bauer, S. J.; Tornabene, B. J.; Hoverman, J. T.;
413 Sepúlveda, M. S. Acute and Chronic Effects of Perfluoroalkyl Substance Mixtures on Larval
414 American Bullfrogs (Rana Catesbeiana). *Chemosphere* **2019**, *236*, 124350.
415 https://doi.org/10.1016/j.chemosphere.2019.124350.

416

417 12. Brase, R. A.; Mullin, E. J.; Spink, D. C. Legacy and Emerging Per- and Polyfluoroalkyl
418 Substances: Analytical Techniques, Environmental Fate, and Health Effects. *IJMS* **2021**, *22* (3),
419 995. https://doi.org/10.3390/ijms22030995.

420

421 13. Zarębska, M.; Bajkacz, S. Poly– and Perfluoroalkyl Substances (PFAS) - Recent Advances
422 in the Aquatic Environment Analysis. *TrAC Trends in Analytical Chemistry* **2023**, *163*, 117062.
423 https://doi.org/10.1016/j.trac.2023.117062.

424

425 14. Liu, Y.; D'Agostino, L. A.; Qu, G.; Jiang, G.; Martin, J. W. High-Resolution Mass Spectrometry
426 (HRMS) Methods for Nontarget Discovery and Characterization of Poly- and per-Fluoroalkyl
427 Substances (PFASs) in Environmental and Human Samples. *TrAC Trends in Analytical Chemistry*
428 **2019**, *121*, 115420. https://doi.org/10.1016/j.trac.2019.02.021.

429

430 15. Dodds, J. N.; Hopkins, Z. R.; Knappe, D. R. U.; Baker, E. S. Rapid Characterization of Per-
431 and Polyfluoroalkyl Substances (PFAS) by Ion Mobility Spectrometry–Mass Spectrometry (IMS-
432 MS). *Anal. Chem.* **2020**, *92* (6), 4427–4435. https://doi.org/10.1021/acs.analchem.9b05364.

433

434 16. Darie-Ion, L.; Whitham, D.; Jayathirtha, M.; Rai, Y.; Neagu, A.-N.; Darie, C. C.; Petre, B. A.
435 Applications of MALDI-MS/MS-Based Proteomics in Biomedical Research. *Molecules* **2022**, *27*
436 (19), 6196. https://doi.org/10.3390/molecules27196196.

437

438 17. Ucal, Y.; Durer, Z. A.; Atak, H.; Kadioglu, E.; Sahin, B.; Coskun, A.; Baykal, A. T.; Ozpinar, A.
439 Clinical Applications of MALDI Imaging Technologies in Cancer and Neurodegenerative
440 Diseases. *Biochimica et Biophysica Acta (BBA) - Proteins and Proteomics* **2017**, *1865* (7), 795–
441 816. https://doi.org/10.1016/j.bbapap.2017.01.005.

442

443 18. Djambazova, K. V.; Klein, D. R.; Migas, L. G.; Neumann, E. K.; Rivera, E. S.; Van De Plas,
444 R.; Caprioli, R. M.; Spraggins, J. M. Resolving the Complexity of Spatial Lipidomics Using MALDI
445 TIMS Imaging Mass Spectrometry. *Anal. Chem.* **2020**, *92* (19), 13290–13297.
446 https://doi.org/10.1021/acs.analchem.0c02520.

447

448 19. Bian, Y.; He, M.-Y.; Ling, Y.; Wang, X.-J.; Zhang, F.; Feng, X.-S.; Zhang, Y.; Xing, S.-G.; Li,
449 J.; Qiu, X.; Li, Y.-R. Tissue Distribution Study of Perfluorooctanoic Acid in Exposed Zebrafish
450 Using MALDI Mass Spectrometry Imaging. *Environmental Pollution* ***2022, 293, 118505.***
451 ***https://doi.org/10.1016/j.envpol.2021.118505***.

452

453 20. Yang, C.; Lee, H. K.; Zhang, Y.; Jiang, L.-L.; Chen, Z.-F.; Chung, A. C. K.; Cai, Z. In Situ
454 Detection and Imaging of PFOS in Mouse Kidney by Matrix-Assisted Laser Desorption/Ionization
455 Imaging Mass Spectrometry. *Anal. Chem.* ***2019, 91 (14), 8783–8788.***
456 ***https://doi.org/10.1021/acs.analchem.9b00711***.

457

458 21. Chen, Y.; Jiang, L.; Zhang, R.; Shi, Z.; Xie, C.; Hong, Y.; Wang, J.; Cai, Z. Spatially Revealed
459 Perfluorooctane Sulfonate-Induced Nephrotoxicity in Mouse Kidney Using Atmospheric Pressure
460 MALDI Mass Spectrometry Imaging. *Science of The Total Environment* ***2022, 838, 156380.***
461 ***https://doi.org/10.1016/j.scitotenv.2022.156380***.

462

463 22. Li, X.; Li, T.; Wang, Z.; Wei, J.; Liu, J.; Zhang, Y.; Zhao, Z. Distribution of Perfluorooctane
464 Sulfonate in Mice and Its Effect on Liver Lipidomic. *Talanta* **2021, *226, 122150.***
465 ***https://doi.org/10.1016/j.talanta.2021.122150***.

466

467 23. Cao, D.; Wang, Z.; Han, C.; Cui, L.; Hu, M.; Wu, J.; Liu, Y.; Cai, Y.; Wang, H.; Kang, Y.
468 Quantitative Detection of Trace Perfluorinated Compounds in Environmental Water Samples by
469 Matrix-Assisted Laser Desorption/Ionization-Time of Flight Mass Spectrometry with 1,8-
470 Bis(Tetramethylguanidino)-Naphthalene as Matrix. *Talanta* **2011, *85 (1), 345–352.***
471 ***https://doi.org/10.1016/j.talanta.2011.03.062***

472

473 24. Jia, S.; Marques Dos Santos, M.; Li, C.; Snyder, S. A. Recent Advances in Mass Spectrometry
474 Analytical Techniques for Per- and Polyfluoroalkyl Substances (PFAS). Anal Bioanal Chem 2022,
475 414 (9), 2795–2807. https://doi.org/10.1007/s00216-022-03905-y.

476

477 25. Dodds, J. N.; Baker, E. S. Ion Mobility Spectrometry: Fundamental Concepts, Instrumentation,
478 Applications, and the Road Ahead. *J. Am. Soc. Mass Spectrom.* **2019**, *30* (11), 2185–2195.
479 https://doi.org/10.1007/s13361-019-02288-2.

480

481 26. Burnum-Johnson, K. E.; Zheng, X.; Dodds, J. N.; Ash, J.; Fourches, D.; Nicora, C. D.;
482 Wendler, J. P.; Metz, T. O.; Waters, K. M.; Jansson, J. K.; Smith, R. D.; Baker, E. S. Ion Mobility
483 Spectrometry and the Omics: Distinguishing Isomers, Molecular Classes and Contaminant Ions
484 in Complex Samples. *TrAC Trends in Analytical Chemistry* **2019**, *116*, 292–299.
485 https://doi.org/10.1016/j.trac.2019.04.022.

486

487 27. Rivera, E. S.; Djambazova, K. V.; Neumann, E. K.; Caprioli, R. M.; Spraggins, J. M. Integrating
488 Ion Mobility and Imaging Mass Spectrometry for Comprehensive Analysis of Biological Tissues:
489 A Brief Review and Perspective. *J Mass Spectrom* **2020**, e4614.
490 https://doi.org/10.1002/jms.4614.

491

492 28. Foster, M.; Rainey, M.; Watson, C.; Dodds, J. N.; Kirkwood, K. I.; Fernández, F. M.; Baker, E.
493 S. Uncovering PFAS and Other Xenobiotics in the Dark Metabolome Using Ion Mobility
494 Spectrometry, Mass Defect Analysis, and Machine Learning. *Environ. Sci. Technol.* **2022**, *56* (12),
495 9133–9143. https://doi.org/10.1021/acs.est.2c00201.

496

497 29. Ridgeway, M. E.; Lubeck, M.; Jordens, J.; Mann, M.; Park, M. A. Trapped Ion Mobility
498 Spectrometry: A Short Review. *International Journal of Mass Spectrometry* **2018**, *425*, 22–35.
499 https://doi.org/10.1016/j.ijms.2018.01.006.

500

501 30. Spraggins, J. M.; Djambazova, K. V.; Rivera, E. S.; Migas, L. G.; Neumann, E. K.; Fuetterer,
502 A.; Suetering, J.; Goedecke, N.; Ly, A.; Van De Plas, R.; Caprioli, R. M. High-Performance
503 Molecular Imaging with MALDI Trapped Ion-Mobility Time-of-Flight (TimsTOF) Mass
504 Spectrometry. *Anal. Chem.* **2019**, *91* (22), 14552–14560.
505 https://doi.org/10.1021/acs.analchem.9b03612.

506

507 31. Calvano, C. D.; Monopoli, A.; Cataldi, T. R. I.; Palmisano, F. MALDI Matrices for Low
508 Molecular Weight Compounds: An Endless Story? *Anal Bioanal Chem* **2018**, *410* (17), 4015–
509 4038. https://doi.org/10.1007/s00216-018-1014-x.

510

511   32. van Kampen, J. J. A.; Burgers, P. C.; de Groot, R.; Gruters, R. A.; Luider, T. M. Biomedical
512   Application of MALDI Mass Spectrometry for Small-Molecule Analysis. *Mass Spectrometry*
513   *Reviews* **2011**, *30* (1), 101–120. https://doi.org/10.1002/mas.20268.
514
515   33. Crotti, S.; Menicatti, M.; Pallecchi, M.; Bartolucci, G. Tandem Mass Spectrometry Approaches
516   for Recognition of Isomeric Compounds Mixtures. *Mass Spectrometry Reviews* **2023**, *42* (4),
517   1244–1260. https://doi.org/10.1002/mas.21757.
518